A statistical modeling framework to assess cross-frequency coupling while accounting for confounding effects

Jessica Nadalin[1], **Louis-Emmanuel Martinet**[2], **Ethan Blackwood**[3], **Meng-Chen Lo**[3], **Alik S. Widge**[3], **Sydney S. Cash**[2], **Uri T. Eden**[1], **Mark A. Kramer**[1*]

***For correspondence:** mak@bu.edu ( )

[1]Department of Mathematics and Statistics, Boston University, Boston, Massachusetts 02215, USA; [2]Department of Neurology, Massachusetts General Hospital, Boston, Massachusetts 02114, USA; [3]Department of Psychiatry, Massachusetts General Hospital, Boston, MA, 02129, USA

Abstract

Cross frequency coupling (CFC) is emerging as a fundamental feature of brain activity, correlated with brain function and dysfunction. Many different types of CFC have been identified through application of numerous data analysis methods, each developed to characterize a specific CFC type. Choosing an inappropriate method weakens statistical power and introduces opportunities for confounding effects. To address this, we propose a statistical modeling framework to estimate high frequency amplitude as a function of both the low frequency amplitude and low frequency phase; the result is a measure of phase-amplitude coupling that accounts for changes in the low frequency amplitude. We show in simulations that the proposed method successfully detects CFC between the low frequency phase or amplitude and the high frequency amplitude, and outperforms an existing method in biologically-motivated examples. Applying the method to *in vivo* data, we illustrate how CFC evolves during seizures and is affected by electrical stimuli.

Introduction

Brain rhythms - as recorded in the local field potential (LFP) or scalp electroencephalogram (EEG) - are believed to play a critical role in coordinating brain networks. By modulating neural excitability, these rhythmic fluctuations provide an effective means to control the timing of neuronal firing [20, 8]. Oscillatory rhythms have been categorized into different frequency bands (e.g., theta [4-10 Hz], gamma [30-80 Hz]) and associated with many functions: the theta band with memory, plasticity, and navigation [20]; the gamma band with local coupling and competition [34, 5]. In addition, gamma and high-gamma (80-200 Hz) activity have been identified as surrogate markers of neuronal firing [48, 42, 23, 47, 69, 50], observable in the EEG and LFP.

In general, lower frequency rhythms engage larger brain areas and modulate spatially localized fast activity [6, 11, 64, 38, 37]. For example, the phase of low frequency rhythms has been shown to modulate and coordinate neural spiking [63, 26, 22] via local circuit mechanisms that provide discrete windows of increased excitability. This interaction, in which fast activity is coupled to slower rhythms, is a common type of cross-frequency coupling (CFC). This particular type of CFC has been shown to carry behaviorally relevant information (e.g., related to position [28, 1], memory [53], decision making and coordination [17, 46, 73, 25]). More generally, CFC has been observed in many brain areas [6, 11, 16, 59, 21, 9], and linked to specific circuit and dynamical mechanisms [26]. The degree of CFC in those areas has been linked to working memory, neuronal computation,

communication, learning and emotion [58, 30, 10, 18, 33, 39, 32, 31, 54], and clinical disorders [24, 72, 66, 3, 19], including epilepsy [68]. Although the cellular mechanisms giving rise to some neural rhythms are relatively well understood (e.g. gamma [71, 70, 40], and theta [58]), the neuronal substrate of CFC itself remains obscure.

Analysis of CFC focuses on relationships between the amplitude, phase, and frequency of two rhythms from different frequency bands. The notion of CFC, therefore, subsumes more specific types of coupling, including: phase-phase coupling (PPC), phase-amplitude coupling (PAC), and amplitude-amplitude coupling (AAC) [26]. PAC has been observed in rat striatum and hippocampus [59] and human cortex [9], AAC has been observed between the alpha and gamma rhythms in visual cortex [27, 29, 55], and between theta and gamma rhythms during spatial navigation [52], and both PAC and AAC have been observed between alpha and gamma rhythms [44]. Many quantitative measures exist to characterize different types of CFC, including: mean vector length or modulation index [9, 57], phase-locking value [21, 36, 61], envelope-to-signal correlation [7], analysis of amplitude spectra [12], coherence between amplitude and signal [15], coherence between the time course of power and signal [44], and eigendecomposition of multichannel covariance matrices [13]. Overall, these different measures have been developed from different principles and made suitable for different purposes, as shown in comparative studies [57, 12, 45, 43].

Despite the richness of this methodological toolbox, it has limitations. For example, because each method focuses on one type of CFC, the choice of method restricts the type of CFC detectable in data. Applying a method to detect PAC in data with both PAC and AAC may: (i) falsely report no PAC in the data, or (ii) miss the presence of significant AAC in the same data. Changes in the low frequency power can also affect measures of PAC; increases in low frequency power can increase the signal to noise ratio of phase and amplitude variables, increasing the measure of PAC, even when the phase-amplitude coupling remains constant [2, 60, 30]. Furthermore, many experimental or clinical factors (e.g., stimulation parameters, age or sex of subject) can impact CFC in ways that are difficult to characterize with existing methods [14]. These observations suggest that an accurate measure of PAC would control for confounding variables, including the power of low frequency oscillations.

To that end, we propose here a generalized linear model (GLM) framework to assess CFC between the high-frequency amplitude and, simultaneously, the low frequency phase and amplitude. This formal statistical inference framework builds upon previous work [35, 45, 65, 60] to address the limitations of existing CFC measures. In what follows, we show that this framework successfully detects CFC in simulated signals, including cases in which a method lacking the low frequency amplitude predictor fails. We compare this method to the modulation index, and show that in signals with CFC dependent on the low-frequency amplitude, the proposed method detects true CFC that cannot be detected with the modulation index. We apply this framework to *in vivo* recordings from human and rat cortex and show examples of how accounting for AAC reveals changes in PAC over the course of seizure, and how to incorporate new covariates directly into the model framework.

Methods

Estimation of the phase and amplitude envelope

To study CFC we estimate three quantities: the phase of the low frequency signal, ϕ_{low}; the amplitude envelope of the high frequency signal, A_{high}; and the amplitude envelope of the low frequency signal, A_{low}. To do so, we first bandpass filter the data into low frequency (4-7 Hz) and high frequency (100-140 Hz) signals, V_{low} and V_{high}, respectively, using a least-squares linear-phase FIR filter of order 375 for the high frequency signal, and order 50 for the low frequency signal. Here we choose specific high and low frequency ranges of interest, motivated by previous *in vivo* observations [9, 59, 51]. However, we note that this method is flexible and not dependent on this choice. We use the Hilbert transform to compute the analytic signals of V_{low} and V_{high}, and from these compute

the phase and amplitude of the low frequency signal (A_{low} and ϕ_{low}) and the amplitude of the high frequency signal (A_{high}).

Modeling framework to assess CFC

Generalized linear models (GLMs) provide a principled framework to assess CFC [45, 35, 60]. Here, we present four models to analyze different types of CFC.

The PAC model

The *PAC model* relates A_{high}, the response variable, to a linear combination of ϕ_{low}, the predictor variable, expressed in a spline basis:

$$\begin{aligned} A_{\text{high}}|\phi_{\text{low}} &\sim \text{Gamma}[\mu, \nu] \\ \log \mu &= \sum_{k=1}^{n} \beta_k f_k(\phi_{\text{low}}), \end{aligned} \tag{1}$$

where the conditional distribution of A_{high} given ϕ_{low} is modeled as a Gamma random variable with mean parameter μ and shape parameter ν, and β_k are undetermined coefficients, which we refer to collectively as β_{PAC}. We choose this distribution as it guarantees real, positive amplitude values. The functions $\{f_1, \cdots, f_n\}$ correspond to spline basis functions, with n control points equally spaced between 0 and 2π, used to approximate ϕ_{low}. We use a tension parameter of 0.5, which controls the smoothness of the splines. Here, we fix $n = 10$, which is a reasonable choice for smooth PAC with one or two broad peaks [35]. For a more detailed discussion and simulation examples of the PAC model, see [35]. We note that the choices of distribution and link function differ from those in [45, 60], where the normal distribution and identity link are used instead.

The CFC model

The *CFC model* extends the PAC model in Equation 1 by including three additional predictors in the GLM: A_{low}, the low frequency amplitude; and interaction terms between the low frequency amplitude and the low frequency phase: $A_{\text{low}} \sin(\phi_{\text{low}})$, and $A_{\text{low}} \cos(\phi_{\text{low}})$. These new terms allow assessment of phase-amplitude coupling while accounting for linear amplitude-amplitude dependence and more complicated phase-dependent relationships on the low frequency amplitude without introducing many more parameters. Compared to the original PAC model in Equation 1, including these new terms increases the number of variables to $n + 3$, and the length of the coefficient vector β_{CFC} to $n + 3$. These changes result in the following model:

$$\begin{aligned} A_{\text{high}}|\phi_{\text{low}}, A_{\text{low}} &\sim \text{Gamma}[\mu, \nu], \\ \log \mu &= \sum_{k=1}^{n} \beta_k f_k(\phi_{\text{low}}) + \beta_{n+1} A_{\text{low}} + \beta_{n+2} A_{\text{low}} \sin(\phi_{\text{low}}) + \beta_{n+3} A_{\text{low}} \cos(\phi_{\text{low}}). \end{aligned} \tag{2}$$

Here, the conditional distribution of A_{high} given ϕ_{low} and A_{low} is modeled as a Gamma random variable with mean parameter μ and shape parameter ν, and β_k are undetermined coefficients.

The AAC model

The *AAC model* relates the high frequency amplitude to the low frequency amplitude:

$$\begin{aligned} A_{\text{high}}|A_{\text{low}} &\sim \text{Gamma}[\mu, \nu] \\ \log \mu &= \beta_1 + \beta_2 A_{\text{low}}, \end{aligned} \tag{3}$$

where the conditional distribution of A_{high} given A_{low} is modeled as a Gamma random variable with mean parameter μ and shape parameter ν. The predictor consists of a single variable and a constant, and the length of the coefficient vector β_{AAC} is 2.

The null model

The *null model* consists of a single, constant predictor variable. This model has a single parameter (β_{null}) to estimate:

$$\log \mu = \beta_{\text{null}}. \tag{4}$$

Intuitively, the null model in Equation 4 fits the average high frequency amplitude without dependence on the low frequency phase, low frequency amplitude, or any other predictor.

The statistics $\mathbf{R}_{\text{PAC}}$, $\mathbf{R}_{\text{AAC}}$, and $\mathbf{R}_{\text{CFC}}$

We compute three measures of CFC, $\mathbf{R}_{\text{PAC}}$, $\mathbf{R}_{\text{AAC}}$, and $\mathbf{R}_{\text{CFC}}$, which use the four models defined in the previous section. We evaluate each model in the three-dimensional space (ϕ_{low}, A_{low}, A_{high}) and calculate the statistics $\mathbf{R}_{\text{PAC}}$, $\mathbf{R}_{\text{AAC}}$, and $\mathbf{R}_{\text{CFC}}$ as the maximum absolute fractional difference between the *null model* mean response function and the *PAC, AAC,* and *CFC models'* mean response functions, respectively. We use the MATLAB function *fitglm* to estimate the models; we note that this procedure estimates the dispersion directly for the gamma distribution.

To compute $\mathbf{R}_{\text{PAC}}$, $\mathbf{R}_{\text{AAC}}$, and $\mathbf{R}_{\text{CFC}}$, we first evaluate the *null model*. We do so by estimating the coefficient β_{null} and computing the mean response function S_{null} of the null model in the three-dimensional (ϕ_{low}, A_{low}, A_{high}) space, which appears as a flat plane (Figure 1A, red).

To compute $\mathbf{R}_{\text{PAC}}$, the statistic characterizing PAC, we first estimate the coefficients β_{PAC} from the *PAC model*. From this, we then compute estimates for the high frequency amplitude using the *PAC model* with 100 evenly spaced values of ϕ_{low} between $-\pi$ and π. Evaluating the *PAC model* in this way results in a mean response function C_{PAC}. We extend this PAC curve C_{PAC} in the A_{low} dimension to create a surface S_{PAC} in the three-dimensional (ϕ_{low}, A_{low}, A_{high}) space (Figure 1A, blue). The surface S_{PAC} has the same structure as the curve C_{PAC} in the (ϕ_{low}, A_{high}) space, and remains constant along the dimension A_{low}. From this, we compute $\mathbf{R}_{\text{PAC}}$ as

$$\mathbf{R}_{\text{PAC}} = \max\left[\text{abs}[1 - S_{\text{PAC}}/S_{\text{null}}]\right], \tag{5}$$

or the maximum absolute fractional difference between the null and PAC mean response functions S_{null} and S_{PAC}. Intuitively, a low value of $\mathbf{R}_{\text{PAC}}$ indicates an absence of PAC, while a high value of $\mathbf{R}_{\text{PAC}}$ indicates the presence of PAC.

Similarly, we compute the $\mathbf{R}_{\text{AAC}}$ statistic, which characterizes AAC, by first estimating the coefficient vector β_{AAC} from the *AAC model*. We then find the corresponding estimate for high frequency amplitude for 640 evenly spaced values between the 5th and 95th quantiles of A_{low} observed; we choose these quantiles to avoid extremely small or large values of A_{low}. This creates a mean response function which appears as a curve C_{AAC} in the two-dimensional (A_{low}, A_{high}) space. We extend this two-dimensional curve to a three-dimensional surface S_{AAC} in the (ϕ_{low}, A_{low}, A_{high}) space which extends C_{AAC} along the ϕ_{low} dimension (Figure 1B). We use this surface to compute $\mathbf{R}_{\text{AAC}}$ as

$$\mathbf{R}_{\text{AAC}} = \max\left[\text{abs}[1 - S_{\text{AAC}}/S_{\text{null}}]\right], \tag{6}$$

or the maximum absolute fractional difference between the null and AAC mean response functions S_{null} and S_{AAC}. Again, a low value of $\mathbf{R}_{\text{AAC}}$ indicates an absence of AAC, while a high value indicates the presence of AAC.

Finally, we compute the statistic $\mathbf{R}_{\text{CFC}}$, which characterizes CFC, using a similar procedure to those developed for $\mathbf{R}_{\text{PAC}}$ and $\mathbf{R}_{\text{AAC}}$. We first compute estimates of the parameters β_{CFC} for the *CFC model*. Again, we find corresponding estimates for A_{high} by fixing A_{low} at one of 640 evenly spaced values between the 5th and 95th quantiles of A_{low} observed and computing the corresponding high frequency amplitude values from the CFC model over 100 evenly spaced values of ϕ_{low} between $-\pi$ and π. This creates a two-dimensional curve C_{CFC} in the two-dimensional (ϕ_{low}, A_{high}) space with fixed A_{low}. We repeat this procedure for all 640 values of A_{low} to create a surface S_{CFC} in the three-dimensional space (ϕ_{low}, A_{low}, A_{high}); see Figure 1C.

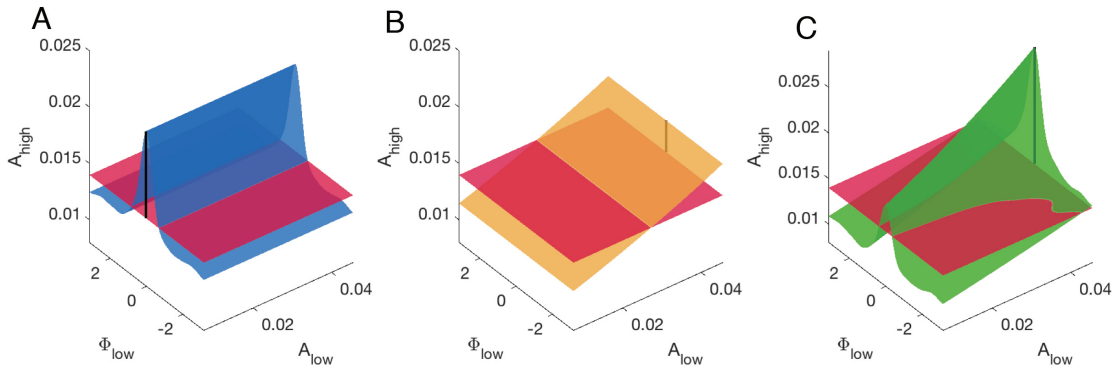

Figure 1. Assessment of PAC, AAC, and CFC in the statistical modeling framework. (A) S_{PAC} (blue) and S_{null} (red) mean response functions in the three-dimensional space (ϕ_{low}, A_{low}, A_{high}). Neither surface varies with A_{low}. **(B)** S_{AAC} (orange) and S_{null} (red) mean response functions from the *AAC model* and *null model* in the three-dimensional space (ϕ_{low}, A_{low}, A_{high}). Neither surface varies with ϕ_{low}. **(C)** S_{CFC} (green) and S_{null} (red) mean response functions in the three-dimensional space (ϕ_{low}, A_{low}, A_{high}). The CFC surface varies with both ϕ_{low} and A_{low}.

We define $\mathbf{R}_{\mathrm{CFC}}$ as the maximum fractional distance between the null surface and CFC surface. We compute the statistic $\mathbf{R}_{\mathrm{CFC}}$ as

$$\mathbf{R}_{\mathrm{CFC}} = \max\left[\mathrm{abs}[1 - S_{\mathrm{CFC}}/S_{\mathrm{null}}]\right], \tag{7}$$

i.e., the maximum absolute fractional difference between the null and CFC surfaces in the three-dimensional space (ϕ_{low}, A_{low}, A_{high}); see Figure 1C.

Estimating 95% confidence intervals for $\mathbf{R}_{\mathrm{PAC}}$, $\mathbf{R}_{\mathrm{AAC}}$, and $\mathbf{R}_{\mathrm{CFC}}$

We compute 95% confidence intervals for $\mathbf{R}_{\mathrm{PAC}}$, $\mathbf{R}_{\mathrm{AAC}}$, and $\mathbf{R}_{\mathrm{CFC}}$ via a parametric bootstrap method [35]. Given a vector of estimated coefficients β_x for $x = \{\text{PAC, AAC, or CFC}\}$, we use its estimated covariance and estimated mean to generate 10,000 normally distributed coefficient sample vectors β_x^j, $j \in \{0, \ldots, 10000\}$, $x = \{\text{PAC, AAC, or CFC}\}$. For each β_x^j, we then compute the high frequency amplitude values from the PAC, AAC, or CFC model, S_x^j. Finally, we compute the $\mathbf{R}_x$ statistic for each j as

$$\mathbf{R}_x^j = \max\left[\mathrm{abs}[1 - S_x^j/S_{\mathrm{null}}]\right]. \tag{8}$$

We note that in this procedure we use the value of S_{null} estimated from the data. The 95% confidence intervals for the statistic are the values of $\mathbf{R}_x^j$ at the 0.025 and 0.975 quantiles [35].

Assessing significance of AAC, PAC, and CFC with analytic p-values

To assess whether evidence exists for significant CFC - present as PAC, AAC, or both - we perform three statistical tests. First, to test for significant CFC, we perform a chi-squared test between the null and CFC models, with 12 degrees of freedom, corresponding to the 12 additional parameters in the CFC model compared to the null model. We use a chi-squared test to compare nested models and evaluate whether additional parameters provide a significant improvement in model fit. We note that the null hypothesis (H_0) is that the additional parameters all equal zero, and the alternative hypothesis (H_A) is that at least one of the additional parameters is nonzero. A p-value below 0.05 indicates that at least one of the parameters in the CFC is significantly different from zero, suggesting that coupling of some kind is present. We label this p-value p_{CFC}.

Next, to test for significant AAC, we perform a chi-squared test between the PAC model and CFC model, with three degrees of freedom due to the three additional parameters in the CFC model. We

consider a p-value below 0.05 significant, indicating that at least one of the parameters unique to the CFC is significantly different from zero, i.e., the model is improved by including the low frequency amplitude terms, which provides evidence for amplitude-amplitude coupling. We label this p-value p_{AAC}.

Finally, to test for significant PAC, we perform a chi-squared test between the AAC and CFC models, with 11 degrees of freedom. A p-value below 0.05 signifies that at least one of the parameters unique to the CFC is significantly different from zero, i.e. the model is improved by including the low frequency phase, which provides evidence for phase-amplitude coupling. We label this p-value p_{PAC}.

Assessing significance of AAC, PAC, and CFC with bootstrap p-values

The chi-squared test is an analytic approach to assess the significance of model predictors, and performs well when the mismatch between the data and model is small. However, for real data these assumptions might not hold. This could result in inaccurate - under or over estimates - of significance. To address this, we implement an alternative measure to assess significance using bootstrap p-values.

We implement the bootstrap as follows. Given two signals V_{low} and V_{high}, and the resulting output values $\mathbf{R}_{\text{PAC}}$, $\mathbf{R}_{\text{AAC}}$, and $\mathbf{R}_{\text{CFC}}$, we apply the Amplitude Adjusted Fourier Transform (AAFT) algorithm [56] on V_{high} to generate a surrogate signal V^i_{high}. In the AAFT algorithm, we first reorder the values of V_{high} by creating a random Gaussian signal W and ordering the values of V_{high} to match W. For example, if the highest value of W occurs at index j, then the highest value of V_{high} will be reordered to occur at index j. Next, we apply the Fourier Transform (FT) to the reordered V_{high} and randomize the phase of the frequency domain signal. This signal is then inverse Fourier transformed and rescaled to have the same amplitude distribution as the original signal V_{high}. In this way, the algorithm produces a permutation V^i_{high} of V_{high} such that the power spectrum and amplitude distribution of the original signal are preserved.

We create 1000 such surrogate signals V^i_{high}, and calculate $\mathbf{R}^i_{\text{PAC}}$, $\mathbf{R}^i_{\text{AAC}}$, and $\mathbf{R}^i_{\text{CFC}}$ between V_{low} and each V^i_{high}. We define our p-values p_{PAC}, p_{AAC}, and p_{CFC} as the proportion of values in $\{\mathbf{R}^i_{\text{PAC}}\}_{i=1}^{1000}$, $\{\mathbf{R}^i_{\text{AAC}}\}_{i=1}^{1000}$, and $\{\mathbf{R}^i_{\text{CFC}}\}_{i=1}^{1000}$ greater than the original values $\mathbf{R}_{\text{PAC}}$, $\mathbf{R}_{\text{AAC}}$, and $\mathbf{R}_{\text{CFC}}$, respectively. If the proportion is zero, we set $p = 0.0005$. We show in Results that this method performs well in all stimulation scenarios considered.

We calculate p-values for the modulation index (MI) in this same way. The modulation index calculates the distribution of high frequency amplitudes versus low frequency phases and measures the distance from this distribution to a uniform distribution of amplitudes. Given the signals V_{low} and V_{high}, and the resulting modulation index value **MI** between them, we calculate the **MI** between V_{low} and 1000 surrogate permutations of V_{high} using the AAFT algorithm. We set p_{MI} to be the proportion of these resulting values greater than the original value **MI**.

Summary of the Modeling Framework

We summarize the model estimation framework (Figure 2) as follows: Given a high frequency signal V_{high} and a low frequency signal V_{low}, if $p_{\text{CFC}} > 0.05$, we conclude there is no statistically significant evidence for CFC in the data. If $p_{\text{CFC}} < 0.05$, we conclude there is statistically significant evidence for CFC, and examine the values p_{AAC} and p_{PAC}. If $p_{\text{AAC}} < 0.05$ and $p_{\text{PAC}} > 0.05$, we conclude there is statistically significant evidence for AAC but not PAC. If $p_{\text{AAC}} > 0.05$ and $p_{\text{PAC}} < 0.05$, we conclude there is statistically significant evidence for PAC but not AAC. Finally, if $p_{\text{AAC}} < 0.05$ and $p_{\text{PAC}} < 0.05$, we conclude there is statistically significant evidence for both PAC and AAC.

Synthetic Time Series with PAC

We construct synthetic time series to examine the performance of the CFC model as follows. First, we simulate 20 s of pink noise data such that the power spectrum scales as $1/f$. We then filter these data into low (4-7 Hz) and high (100-140 Hz) frequency bands, as described in *Methods: Estimation*

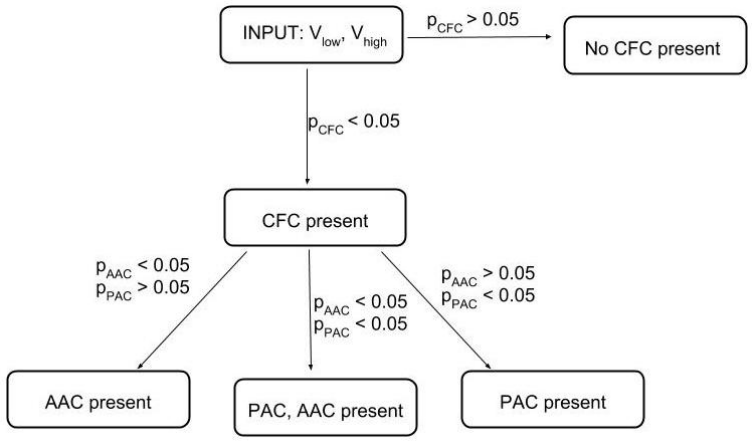

Figure 2. Illustration of the statistical modeling framework. From two input signals V_{low} and V_{high}, if evidence for CFC appears ($p_{\text{CFC}} < 0.05$), then evidence for significant PAC ($p_{\text{PAC}} < 0.05$) and AAC ($p_{\text{AAC}} < 0.05$) is examined.

of the phase and amplitude envelope, creating signals V_{low} and V_{high}. Next, we couple the amplitude of the high frequency signal to the phase of the low frequency signal. To do so, we first locate the peaks of V_{low} and determine the times $t_k,\ k = \{1, 2, 3, \ldots, K\}$, of the K relative extrema. We note that these times correspond to $\phi_{\text{low}} = 0$. We then create a smooth modulation signal **M** which consists of a 42 ms Hanning window of height $1 + I_{\text{PAC}}$ centered at each t_k, and a value of 1 at all other times (Figure 3A). The intensity parameter I_{PAC} in the modulation signal corresponds to the strength of PAC. $I_{\text{PAC}} = 0.0$ corresponds to no PAC, while $I_{\text{PAC}} = 1.0$ results in a 100% increase in the high frequency amplitude at each t_k, creating strong PAC. We create a new signal V'_{high} with the same phase as V_{high}, but with amplitude dependent on the phase of V_{low} by setting

$$A_{\text{high}} = \mathbf{M}$$
$$V'_{\text{high}} = 0.01 * A_{\text{high}} * \cos(\phi_{\text{high}})\,.$$

We create the final voltage trace V as

$$V = V_{\text{low}} + V'_{\text{high}} + c * V_{\text{pink}}$$

where V_{pink} is a new instance of pink noise multiplied by a small constant $c = 0.01$. In the signal V, brief increases of the high frequency activity occur at a specific phase (0 radians) of the low frequency signal.

Synthetic Time Series with AAC

To generate synthetic time series with dependence on the low frequency amplitude, we follow the procedure in the preceding section to generate V_{low}, V_{high}, and A_{low}. We then induce amplitude-amplitude coupling between the low and high frequency components by creating a new signal V^*_{high} such that

$$V^*_{\text{high}} = V_{\text{high}}\left(1 + I_{\text{AAC}}\frac{A_{\text{low}}}{\max\left(A_{\text{low}}\right)}\right),$$

where I_{AAC} is the intensity parameter corresponding to the strength of amplitude-amplitude coupling. We define the final voltage trace V as

$$V = V_{\text{low}} + V^*_{\text{high}} + c * V_{\text{pink}}$$

where V_{pink} is a new instance of pink noise multiplied by a small constant $c = 0.01$ (Figure 3B).

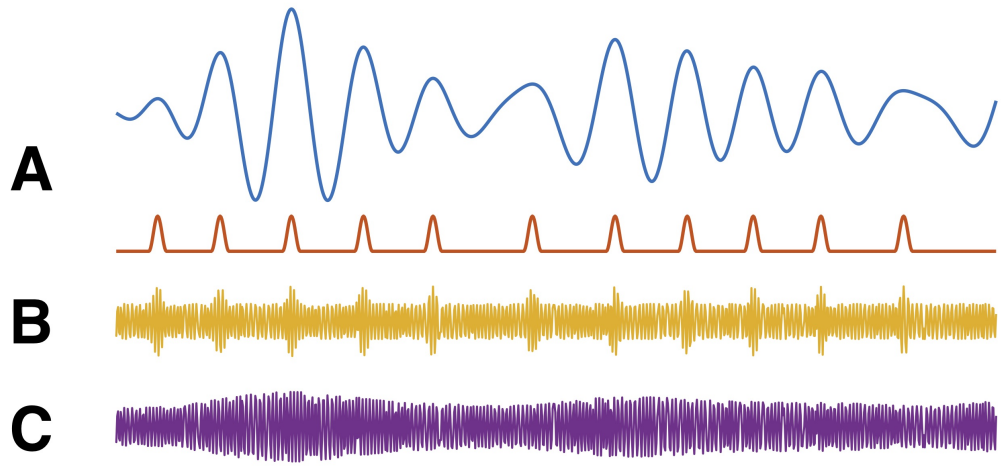

Figure 3. (A) Example simulation of V_{low} (blue) and modulation signal **M** (red). When the phase of V_{low} is 0 radians, **M** increases. **(B)** Example simulation of PAC. When the phase of V_{low} is 0 radians, the high frequency amplitude (yellow) increases. **(C)** Example simulations of AAC. When the amplitude of V_{low} is large, so is the amplitude of the high frequency signal (purple).

Code Availability

The code to perform this analysis is available for reuse and further development at https://github.com/Eden-Kramer-Lab/GLM-CFC .

Results

We first examine the performance of the CFC measure through simulation examples, using analytic p-values. In doing so, we show that the statistics $\mathbf{R}_{\text{CFC}}$, $\mathbf{R}_{\text{PAC}}$, and $\mathbf{R}_{\text{AAC}}$ accurately detect different types of cross-frequency coupling, increase with the intensity of coupling, and detect weak PAC coupled to the low frequency amplitude. We show that the proposed method is less sensitive to changes in low frequency power, and outperforms an existing PAC measure that lacks dependence on the low frequency amplitude. We conclude with an example application to human microelectrode array recordings during seizure, and propose that the $\mathbf{R}_{\text{CFC}}$ measure identifies CFC not detected in a standard PAC measure.

The absence of CFC produces no significant detections of coupling

We first consider simulated signals without CFC. To create these signals, we follow the procedure in *Methods: Synthetic Time Series with PAC* with the modulation intensity set to zero ($I_{\text{PAC}} = 0$). In the resulting signals, A_{high} is approximately constant and does not depend on ϕ_{low} or A_{low}. We estimate the null, PAC, AAC, and CFC models from these data; we show example fits of the model surfaces in Figures 4B. We observe that the PAC, AAC, and CFC models exhibit small modulations in the estimated high frequency amplitude envelope as a function of the low frequency phase and amplitude.

To assess the distribution of significant **R** values in the case of no cross-frequency coupling, we simulate 1000 instances of the pink noise signals (each of 20 s) and apply the null, PAC, AAC, and CFC models to each instance, plotting significant **R** values in Figure 4C. We find that for all 1000 instances, p_{CFC}, p_{PAC}, and p_{AAC} are greater than 0.05, indicating no evidence of significant AAC or PAC in these simulated data, as expected.

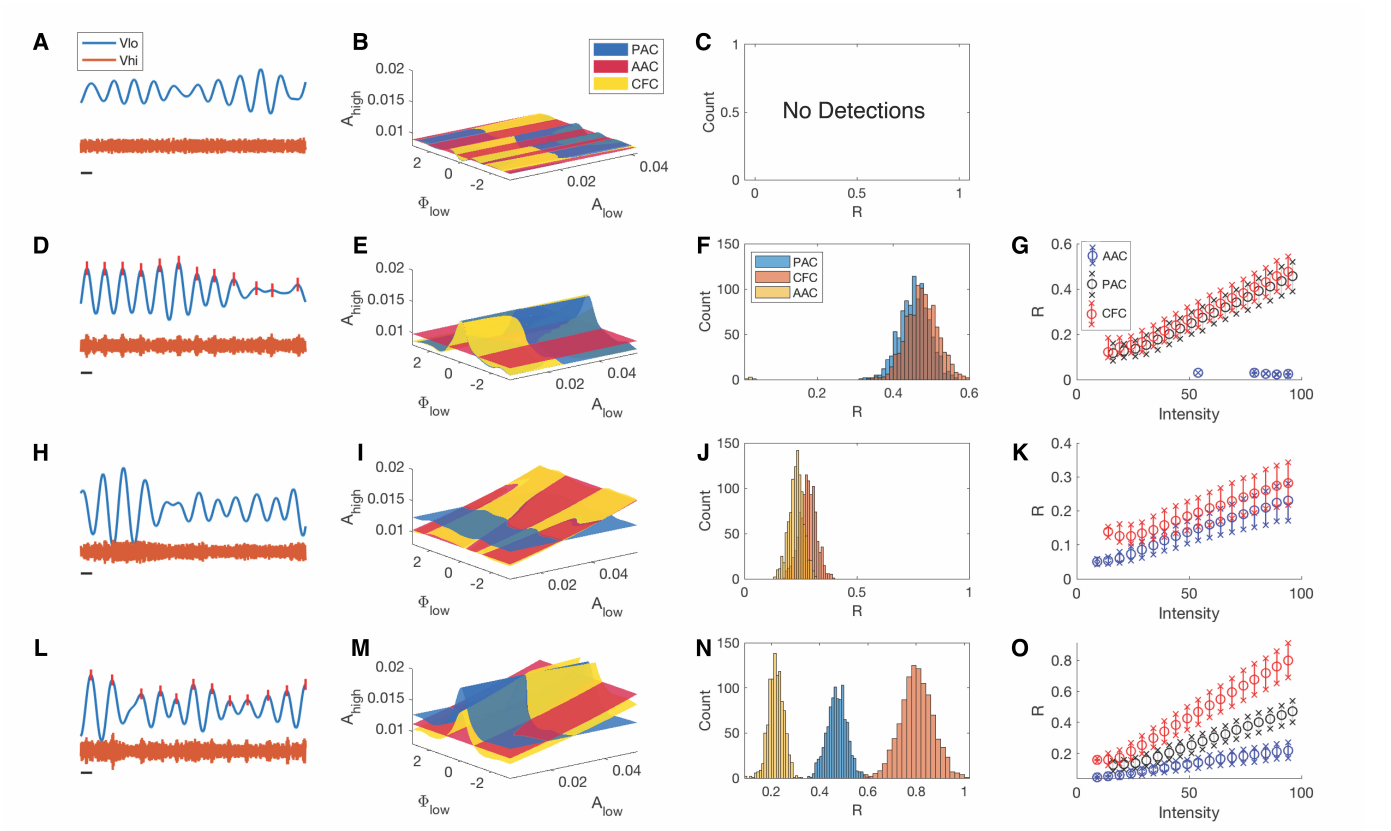

Figure 4. The statistical modeling framework successfully detects different types of cross-frequency coupling. (A-C) Simulations with no CFC. (A) When no CFC occurs, the low frequency signal (blue) and high frequency signal (orange) evolve independently. (B) The model fits for $\mathbf{R}_{PAC}$, $\mathbf{R}_{AAC}$, and $\mathbf{R}_{CFC}$ suggest no dependence of A_{high} on ϕ_{low} or A_{low}. (C) Significant (p<0.05) values of $\mathbf{R}_{PAC}$, $\mathbf{R}_{AAC}$, and $\mathbf{R}_{CFC}$ from 1000 simulations. No significant values for the statistics **R** are detected. **(D-G)** Simulations with PAC only. (D) When the phase of the low frequency signal is near 0 radians (red tick marks), the amplitude of the high frequency signal increases. (E) The model fits for for $\mathbf{R}_{PAC}$, $\mathbf{R}_{AAC}$, and $\mathbf{R}_{CFC}$ suggest dependence of A_{high} on ϕ_{low}. (F) In 1000 simulations, significant values of $\mathbf{R}_{PAC}$ and $\mathbf{R}_{CFC}$ frequently appear, while significant values of $\mathbf{R}_{AAC}$ do not. (G) As the intensity of PAC increases, so do the significant values of $\mathbf{R}_{PAC}$ and $\mathbf{R}_{CFC}$, while any significant values of $\mathbf{R}_{AAC}$ remain small. **(H-K)** Simulations with AAC only. (H) The amplitudes of the high frequency signal and low frequency signal are positively correlated. (I) The model fits for $\mathbf{R}_{PAC}$, $\mathbf{R}_{AAC}$, and $\mathbf{R}_{CFC}$ suggest dependence of A_{high} on A_{low}. (J) In 1000 simulations, significant values of $\mathbf{R}_{AAC}$ and $\mathbf{R}_{CFC}$ frequently appear. (K) As the intensity of AAC increases, so do the significant values of $\mathbf{R}_{AAC}$ and $\mathbf{R}_{CFC}$. No values of $\mathbf{R}_{PAC}$ are found to be significant. **(L-O)** Simulations with PAC and AAC. (L) The amplitude of the high frequency signal increases when the phase of the low frequency signal is near 0 radians and the amplitude of the low frequency signal is large. (M) The model fits for $\mathbf{R}_{PAC}$, $\mathbf{R}_{AAC}$ (red), and $\mathbf{R}_{CFC}$ suggest dependence of A_{high} on ϕ_{low} and A_{low}. (N) In 1000 simulations, significant values of $\mathbf{R}_{PAC}$, $\mathbf{R}_{AAC}$ and $\mathbf{R}_{CFC}$ frequently appear. (O) As the intensity of PAC and AAC increase, so do the significant values of $\mathbf{R}_{PAC}$, $\mathbf{R}_{AAC}$ and $\mathbf{R}_{CFC}$.

The proposed method accurately detects PAC

We next consider signals that possess phase-amplitude coupling, but lack amplitude-amplitude coupling. To do so, we simulate a 20 s signal with A_{high} modulated by ϕ_{low} (Figure 4D); more specifically, A_{high} increases when ϕ_{low} is near 0 radians (see *Methods*, $I_{\text{PAC}} = 1$). We then estimate the null, PAC, AAC, and CFC models from these data; we show example fits in Figure 4E. We find that the PAC and CFC models deviate from the null model at the preferred phase $\phi_{\text{low}} = 0$. We note that, because the data do not depend on the low frequency amplitude (A_{low}), the PAC and CFC models have very similar shapes in the (ϕ_{low}, A_{low}, A_{high}) space, and the AAC model is nearly flat.

Simulating 1000 instances of these 20 s signals with induced phase-amplitude coupling, we find $p_{\text{AAC}} < 0.05$ for only 0.5% of the simulations, while $p_{\text{PAC}}, p_{\text{CFC}} < 0.05$ for 100% of the simulations, indicating that the inclusion of the A_{low} parameter in our model seldom improves the fit. We find that the significant values of $\mathbf{R}_{\text{PAC}}$ and $\mathbf{R}_{\text{CFC}}$ lie well above 0 (Figure 4F), and that as the intensity of the simulated phase-amplitude coupling increases (see Methods), so do the statistics $\mathbf{R}_{\text{PAC}}$ and $\mathbf{R}_{\text{CFC}}$ (Figure 4G), while the few values of spurious significant $\mathbf{R}_{\text{AAC}}$ remain close to 0. We conclude that the proposed method accurately detects the presence of phase-amplitude coupling in these simulated data.

The proposed method accurately detects AAC

We next consider signals with amplitude-amplitude coupling, but without phase-amplitude coupling. We simulate a 20 s signal such that A_{high} is modulated by A_{low} (see *Methods*, $I_{\text{AAC}} = 1$); when A_{low} is large, so is A_{high} (Figure 4H). We then estimate the null, PAC, AAC, and CFC models (example fits in Figure 4I). We find that the AAC model deviates from the null model, increasing along the A_{low} axis, and that the CFC model closely follows this trend, while the PAC model remains mostly flat, as expected.

Simulating 1000 instances of these signals we find that $p_{\text{AAC}}, p_{\text{CFC}} < 0.05$ for 100% of simulations, while $p_{\text{PAC}} < 0.05$ for 0% of simulations, indicating that inclusion of the ϕ_{low} terms in the model do not improve the model fit. The significant values of $\mathbf{R}_{\text{CFC}}$ and $\mathbf{R}_{\text{AAC}}$ are similar, lying above 0 (Figure 4J), and increases in the intensity of AAC produce increases in both $\mathbf{R}_{\text{AAC}}$ and $\mathbf{R}_{\text{CFC}}$ (Figure 4K). We conclude that the proposed method accurately detects the presence of amplitude-amplitude coupling.

The proposed method accurately detects the simultaneous occurrence of PAC and AAC

We now consider signals that possess both phase-amplitude coupling and amplitude-amplitude coupling. To do so, we simulate time series data with both AAC and PAC (Figure 4L). In this case, A_{high} increases when ϕ_{low} is near 0 radians and when A_{low} is large (see *Methods*, $I_{\text{PAC}} = 1$ and $I_{\text{AAC}} = 1$). We then estimate the null, PAC, AAC, and CFC models from the data and visualize the results (Figure 4M). We find that the PAC model deviates from the null model near $\phi_{\text{low}} = 0$, and that the AAC model increases linearly with A_{low}. The CFC model exhibits both of these behaviors, increasing at $\phi_{\text{low}} = 0$ and as A_{low} increases.

Simulating 1000 instances of signals with both AAC and PAC present, we find that p_{AAC}, p_{PAC}, and p_{CFC} are all less than 0.05 in 100% of simulations. The distributions of significant $\mathbf{R}_{\text{PAC}}$, $\mathbf{R}_{\text{AAC}}$, and $\mathbf{R}_{\text{CFC}}$ values lie above 0, consistent with the presence of both PAC and AAC (Figure 4N), and as the intensity of PAC and AAC increases, so do the values of $\mathbf{R}_{\text{PAC}}$, $\mathbf{R}_{\text{AAC}}$, and $\mathbf{R}_{\text{CFC}}$ (Figure 4O). We conclude that the model successfully detects the concurrent presence of PAC and AAC.

The proposed method is less affected by fluctuations in low-frequency amplitude

Increases in low frequency power can increase measures of cross-frequency coupling, although the underlying CFC remains unchanged [2, 14]. Characterizing the impact of this confounding effect is important both to understand measure performance and to produce accurate interpretations of analyzed data. To examine this phenomenon, we perform the following simulation. First, we

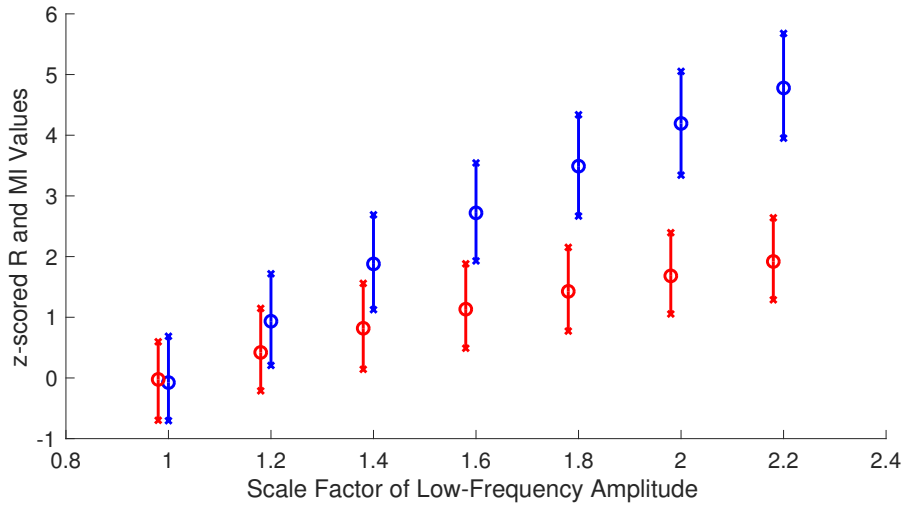

Figure 5. Increases in the amplitude of the low frequency signal increase the modulation index, and less so $\mathbf{R}_{\mathbf{CFC}}$. As the low frequency amplitude increases, so does **MI** (blue) and $\mathbf{R}_{\text{CFC}}$ (red) although the latter increases more slowly. Circles indicate the median and x's the 25th and 75th quantiles at each scale factor. Z-scores were computed using sample means and standard deviations from the condition with scale factor equal to 1.

simulate a signal V with fixed PAC (intensity $I_{\text{PAC}} = 1$, see *Methods*). Second, we filter V into its low and high frequency components V_{low} and V_{high}, respectively. Then, we create a new signal V_k as follows:

$$V_k = k\, V_{\text{low}} + V_{\text{high}} + V_{noise}\,, \tag{9}$$

where k is a value between 1.0 and 2.2, and V_{noise} is a pink noise term (see *Methods*). We note that the value of k only modifies the amplitude of the low frequency component of V and does not alter the PAC. To analyze the CFC in this new signal we compute $\mathbf{R}_{\text{CFC}}$ and a measure of PAC in common use: the modulation index **MI** [57].

We show in Figure 5 population results (1000 realizations of the simulated signal V_k for each k) for the z-scored **R** and **MI** values versus the scale factor k; to compute the z-score we use the mean and standard deviation from the $k = 1$ simulations. We observe that increases in the amplitude of V_{low} produce increases in **MI** and $\mathbf{R}_{\text{CFC}}$. However, this increase is more dramatic for **MI** than for $\mathbf{R}_{\text{CFC}}$. We conclude that the statistic $\mathbf{R}_{\text{CFC}}$ determined from the CFC model — which includes the low frequency amplitude as a predictor in the GLM — is more robust to increases in low frequency power than a method that only includes the low frequency phase.

Sparse PAC is detected when coupled to the low frequency amplitude

While the modulation index has been successfully applied in many contexts [10, 26], instances may exist where this measure is not optimal. For example, because the modulation index was not designed to account for the low frequency amplitude, it may fail to detect CFC when A_{high} depends not only on ϕ_{low}, but also on A_{low}. In what follows, we consider two such instances. In the first, we hypothesize that since the modulation index considers the distribution of A_{high} at all observed values of ϕ_{low}, it may fail to detect coupling events that occur sparsely at only a subset of appropriate ϕ_{low} occurrences. The CFC model, on the other hand, may detect these sparse events if these events are coupled to A_{low}. To test this hypothesis, we consider two simulation scenarios in which PAC occurs sparsely in time.

First, we consider a signal V with PAC, and corresponding modulation signal **M** with intensity value $I_{\text{PAC}} = 1.0$ (see *Methods*, Figure 6A-B). We then modify this signal to reduce the number of PAC

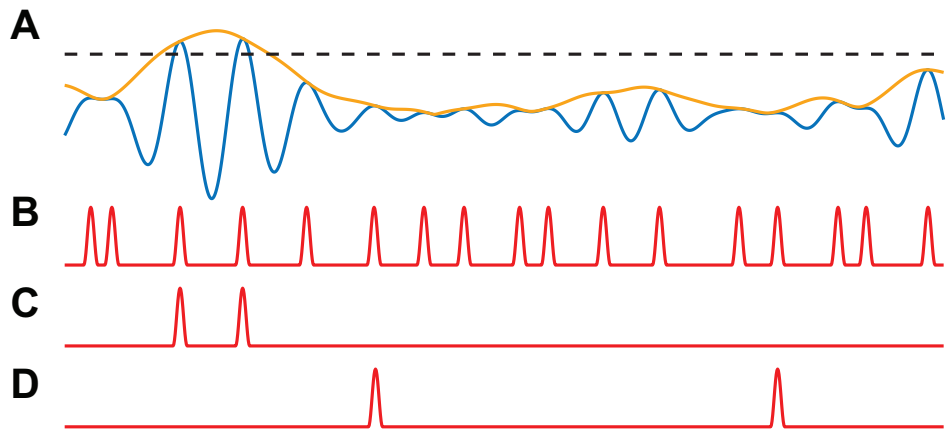

Figure 6. PAC events restricted to a subset of occurrences are still detectable. (A) The low frequency signal (blue), amplitude envelope (yellow), and threshold (black). **(B-D)** The modulation signal increases (B) at every occurrence of $\phi_{\text{low}} = 0$, (C) only when A_{low} exceeds the threshold and $\phi_{\text{low}} = 0$, and (D) at a subset of times when $\phi_{\text{low}} = 0$ and independent of A_{low}.

events in a way that depends on A_{low}. To do so, we preserve PAC at the peaks of V_{low} (i.e., when $\phi_{\text{low}} = 0$), but now only when these peaks are large, more specifically in the top 5% of peak values.

We define a threshold value T to be the 95th quantile of the peak V_{low} values, and modify the modulation signal **M** as follows. When **M** exceeds 1 (i.e., when $\phi_{\text{low}} = 0$) and the low frequency amplitude exceeds T (i.e., $A_{\text{low}} \geq T$), we make no change to **M**. Alternatively, when **M** exceeds 1 and the low frequency amplitude lies below T (i.e., $A_{\text{low}} < T$), we decrease **M** to 1 (Figure 6C). In this way, we create a modified modulation signal $\mathbf{M}_1$ such that in the resulting signal V_1, when $\phi_{\text{low}} = 0$ and A_{low} is large enough, A_{high} is increased; and when $\phi_{\text{low}} = 0$ and A_{low} is not large enough, there is no change to A_{high}. This signal V_1 hence has some number (N) of phase-amplitude coupling events, which is much less than the number of times $\phi_{\text{low}} = 0$. We label this first scenario the dependent case.

Second, we create a signal V_2 with the same number of PAC events (N) as V_1, but without dependence on A_{low}. To do so, we create a new modulation signal $\mathbf{M}_2$ such that $\mathbf{M}_2$ has the same number of peaks (N) as $\mathbf{M}_1$, but these peaks are chosen to occur at $\phi_{\text{low}} = 0$ and random low frequency amplitude values (Figure 6D). The resulting signal V_2 then has the same number of CFC events as V_1, but these events occur at times independent of A_{low}. We call this second scenario the independent case.

We generate 1000 realizations of the simulated signals V_1 and V_2, and from these signals compute $\mathbf{R}_{\text{CFC}}$ and **MI**. We find that in the independent case, i.e., when A_{high} is independent of A_{low}, **MI** detects CFC in 18% of simulations and $\mathbf{R}_{\text{CFC}}$ detects CFC in 25% of simulations. In this scenario, although PAC occurs in the signal V_2, this PAC occurs infrequently, and both methods rarely detect it. In the dependent case, i.e., when A_{high} depends on A_{low}, **MI** detects PAC in only 16% of simulations, while $\mathbf{R}_{\text{CFC}}$ detects CFC in 45% of simulations. In this case, although the PAC still occurs infrequently, these occurrences are coupled to A_{low}, and the CFC model — which includes both A_{low} and ϕ_{low} as predictors — successfully detects these events much more frequently. We conclude that when the PAC is dependent on A_{low}, $\mathbf{R}_{\text{CFC}}$ more accurately detects these sparse coupling events due to the inclusion of the A_{low} predictor in the model.

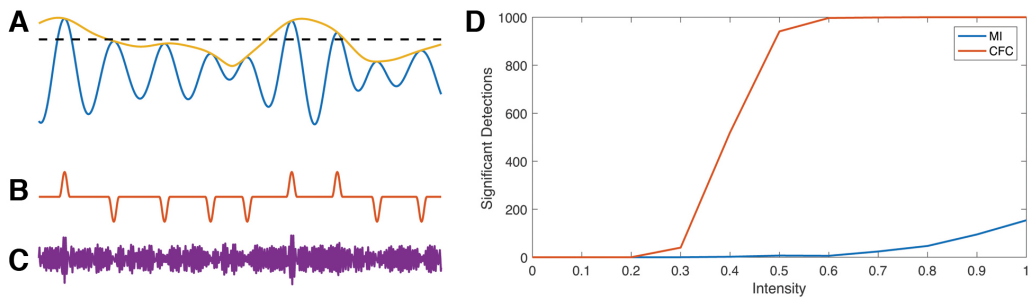

Figure 7. (A) The low frequency signal (blue), amplitude envelope (yellow), and threshold (black). **(B)** The modulation signal (red) increases when $\phi_{\text{low}} = 0$ and $A_{\text{low}} > T$, and deceases when $\phi_{\text{low}} = 0$ and $A_{\text{low}} < T$. **(C)** The modulated A_{high} signal (purple) increases and decreases with the modulation signal. **(D)** Intensity I versus the number of significant detections (out of 1000) for $\mathbf{R}_{\text{CFC}}$ (red) and **MI** (blue). After I exceeds 0.6, $\mathbf{R}_{\text{CFC}}$ detects 100% of simulated CFC, while **MI** never surpasses 20% detection.

The CFC model detects simultaneous PAC and AAC missed in an existing method

As a second example to illustrate the utility of the proposed method, we consider another scenario in which A_{low} impacts the occurrence of PAC. More specifically, we consider a case in which A_{high} increases at a fixed low frequency phase for high values of A_{low}, and A_{high} decreases at the same phase for small values of A_{low}. In this case, we expect that the modulation index may fail to detect the coupling because the distribution of A_{high} over ϕ_{low} would appear uniform when averaged over all values of A_{low}; the dependence of A_{high} on ϕ_{low} would only become apparent after accounting for A_{low}.

To implement this scenario, we consider the modulation signal **M** (see *Methods*) with an intensity value $I_{\text{PAC}} = 1$. We consider all peaks of A_{low} and set the threshold T to be the 50th quantile (Figure 7A). We then modify the modulation signal **M** as follows. When **M** exceeds 1 (i.e., when $\phi_{\text{low}} = 0$) and the low frequency amplitude exceeds T (i.e., $A_{\text{low}} \geq T$), we make no change to **M**. Alternatively, when **M** exceeds 1 and the low frequency amplitude lies below T (i.e. $A_{\text{low}} < T$), we decrease **M** to 0 (Figure 7B). In this way, we create a modified modulation signal **M** such that when $\phi_{\text{low}} = 0$ and A_{low} is large enough, A_{high} is increased; and when $\phi_{\text{low}} = 0$ and A_{low} is small enough, A_{high} is decreased (Figure 7C).

Using this method, we simulate 1000 realizations of this signal at each of 10 values of I between 0 and 1, and calculate **MI** and $\mathbf{R}_{\text{CFC}}$ for each signal (Figure 7D). We find that as the intensity increases, the percentage of significant detections for $\mathbf{R}_{\text{CFC}}$ (i.e. where $p_{\text{CFC}} < 0.05$) approaches 100%, while the percentage of significant detections for **MI**, (i.e., where $p_{\text{MI}} < 0.05$) remains less than 20%. We conclude that the CFC method more accurately detects the combined PAC and AAC in this simulation compared to the modulation index.

An alternative method to assess significance produces consistent results

In the previous sections, we applied an analytic approach to assess the significance of model predictors. This approach is computationally efficient, and performs well in the simulations above in which the mismatch between the data and model is small. Here, we consider an alternative approach of computing p-values - a bootstrap procedure - that is more expensive to compute but requires fewer assumptions about the data. We apply this bootstrap procedure (see *Methods*) to four different scenarios: (i) where no CFC is present, (ii) where PAC but not AAC is present, (iii) where AAC but not PAC is present, and (iv) where PAC and AAC are both present. In the first case, to create a signal with no CFC, we simulate 20 s of pink noise data such that the power spectrum scales as $1/f$. We choose these simulated data to introduce additional variability in the amplitude of the high frequency signal; unlike the simulation in Figure 4A, in which the value of A_{high} was approximately

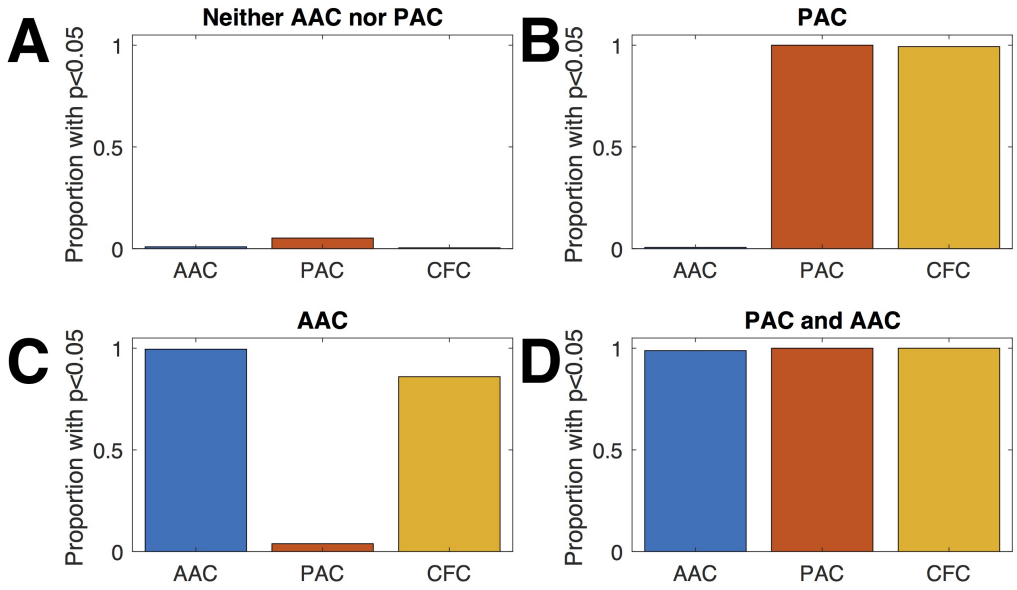

Figure 8. Computing p-values using a bootstrap method produces consistent results. Proportion of simulated signals with p_{AAC}, p_{PAC}, and $p_{\text{CFC}} < 0.05$ when **(A)** Neither PAC nor AAC occurs, **(B)** PAC occurs, **(C)** AAC occurs, and **(D)** both PAC and AAC occur.

constant, the value of A_{high} here is more variable. Computing p_{PAC}, p_{AAC}, and p_{CFC} using the bootstrap method, we find that $p_{\text{CFC}} < 0.05$ for 0.4% of simulations, $p_{\text{PAC}} < 0.05$ for 5.2% of simulations, and $p_{\text{AAC}} < 0.05$ for 0.9% of simulations (Figure 8A). We detect no evidence of CFC, consistent with the lack of CFC in these data.

Next, to simulate a signal with PAC but no AAC, we first follow the procedures in *Methods* to create V_{low}, V_{high}, and the modulation signal **M**. Then, we multiply V_{high} by the modulation signal **M** to create the voltage trace $V = V_{\text{low}} + \mathbf{M}\, V_{\text{high}} + c\, V_{\text{pink}}$, where again V_{pink} is a new instance of pink noise multiplied by a small constant $c = 0.01$. We note that by modulating V_{high} directly by **M**, instead of modulating A_{high} by **M**, we introduce additional variability in the high frequency amplitude that is not dependent on the low frequency signal. We simulate 1000 instances of V, each time measuring p_{PAC}, p_{AAC}, and p_{CFC} using the bootstrap method, and find that $p_{\text{CFC}} < 0.05$ for 99.3% of simulations, $p_{\text{PAC}} < 0.05$ for 100% of simulations, and $p_{\text{AAC}} < 0.05$ for 0.6% of simulations (Figure 8B). Consistent with the constructed signal, we conclude there is PAC, but no AAC, in these simulated data.

We next simulate a signal with AAC, but not PAC. Following the procedures in *Methods: Synthetic Time Series with AAC*, we simulate 1000 instances of V, and in each instance measure p_{PAC}, p_{AAC}, and p_{CFC} using the bootstrap method. We find that $p_{\text{CFC}} < 0.05$ for 86% of simulations, $p_{\text{PAC}} < 0.05$ for 3.9% of simulations, and $p_{\text{AAC}} < 0.05$ for 99.5% of simulations (Figure 8C), consistent with the presence of AAC, but not PAC, in the simulated data.

Finally, to simulate a signal with both PAC and AAC, we multiply V_{high} by the modulation signal **M** to introduce PAC, and then multiply the result by A_{low} to introduce AAC. We create the final voltage trace V as the sum of V_{low}, the PAC and AAC modulated V_{high}, and a new instance of pink noise multiplied by a small constant $(c = 0.01)$. We find that $p_{\text{CFC}} < 0.05$ for 100% of simulations, $p_{\text{PAC}} < 0.05$ for 100% of simulations, and $p_{\text{AAC}} < 0.05$ for 98.8% of simulations (Figure 8D). We conclude that the bootstrap p-values accurately detects the presence of both PAC and AAC in the simulated data.

Application to *in vivo* human seizure data

To evaluate the performance of the proposed method on *in vivo* data, we consider example recordings from human cortex. Two patients (males ages 45, 32 years) with medically intractable

focal epilepsy underwent clinically indicated intracranial cortical recordings for epilepsy monitoring. In addition to clinical electrode implantation, these patients were also implanted with a 10×10 (4 mm × 4 mm) NeuroPort microelectrode array (MEA; Blackrock Microsystems, Utah) in a neocortical area expected to be resected with high probability, in either the middle or superior temporal gyrus. The MEA consist of 96 recording platinum-tipped silicon probes, with a length of either 1-mm or 1.5-mm, corresponding to neocortical layer III as confirmed by histology after resection. The reference electrode was either subdural or epidural, chosen dynamically based on recording quality. Signals from the MEA were acquired continuously at 30 kHz per channel. Seizure onset times were determined by an experienced encephalographer (S.S.C.) through inspection of the macroelectrode recordings, referral to the clinical report, and clinical manifestations recorded on video. For a detailed clinical summary of each patient, see patients P1 and P2 of [67]. This research was approved by local Institutional Review Boards at Massachusetts General Hospital and Brigham Women's Hospitals (Partners Human Research Committee), and at Boston University according to National Institutes of Health guidelines.

Visual inspection of the LFP data (Figure 9A) reveals the emergence of large amplitude voltage fluctuations during the approximately 80 s seizure. To analyze the CFC in these data, we separate this signal into 20 s segments with 10 s overlap, and analyze each segment using the CFC model framework. While little evidence of CFC appears before the seizure (Figure 9A), during the seizure we find significant (using bootstrap p-values) $\mathbf{R}_{\mathrm{PAC}}$, $\mathbf{R}_{\mathrm{AAC}}$, and $\mathbf{R}_{\mathrm{CFC}}$ values.

To further investigate these results, we select a 20 s segment with significant and large $\mathbf{R}_{\mathrm{PAC}}$, $\mathbf{R}_{\mathrm{AAC}}$, and $\mathbf{R}_{\mathrm{CFC}}$ values to examine (Figure 9B). Visual inspection reveals the occurrence of large amplitude, low frequency oscillations and small amplitude, high frequency oscillations. To examine the detected coupling in even more detail, we isolate a 2 s segment (Figure 9C), and display the signal V, the high frequency signal V_{high}, the low frequency phase ϕ_{low}, and the low frequency amplitude A_{low}. We observe that when ϕ_{low} is near π (gray bars in Figure 9C), A_{high} increases, consistent with the presence of PAC and a significant value of $\mathbf{R}_{\mathrm{PAC}}$. Examining the low frequency amplitude A_{low} and high frequency amplitude A_{high} over the same 20 s segment (Figure 9D), we find that A_{low} and A_{high} increase together, consistent the presence of AAC and a significant value of $\mathbf{R}_{\mathrm{AAC}}$.

Repeating this analysis for a seizure recorded from a second patient (Figure 10A), we again find significant $\mathbf{R}_{\mathrm{PAC}}$, $\mathbf{R}_{\mathrm{AAC}}$, and $\mathbf{R}_{\mathrm{CFC}}$ values during the seizure (Figure 10A). Selecting a 20 s segment with large and significant $\mathbf{R}_{\mathrm{PAC}}$, $\mathbf{R}_{\mathrm{AAC}}$, and $\mathbf{R}_{\mathrm{CFC}}$ values (Figure 10B), and isolating a 1 s interval from this segment (Figure 10C), we observe evidence of PAC and AAC. We find that near $\phi_{\mathrm{low}} = 0$, there is an increase in A_{high} at two time points (grey bars in Figure 10C) consistent with the presence of PAC. However, at other times when the phase is near $\phi_{\mathrm{low}} = 0$, we observe no increase in A_{high}, consistent with a lack of PAC. We note that the value of A_{low} distinguishes these scenarios; when we observe PAC, A_{low} is large, whereas when we do not observe PAC, A_{low} is small. Hence, the increase in A_{high} is related not only to ϕ_{low}, but also A_{low}, i.e., there is also AAC in these data, consistent with the detection of significant PAC and AAC values.

Application to *in vivo* rodent data during electrical stimulation

As a second example to illustrate the performance of the new method, we consider LFP recordings from from the infralimbic cortex (IL) and basolateral amygdala (BLA) of an outbred Long-Evans rat before and after the delivery of an experimental electrical stimulation intervention described in [4]. 8 microwires in each region, referenced as bipolar pairs, sampled each region's LFP at 30 kHz. The electrical stimulation was explicitly expected to change inter-regional coupling (see [4] for a detailed description of the experiment). Here we examine how cross-frequency coupling between low frequency (5-8 Hz) IL signals and high frequency (70-110 Hz) BLA signals changes from the pre-stimulus (*pre*) to the post-stimulus (*post*) condition. To do so, we filter the data V into low and high frequency signals using the techniques from *Methods*, and compute the MI and $\mathbf{R}_{\mathrm{CFC}}$ between each possible BLA-IL pairing, sixteen in total (Figure 11).

For the **MI**, we find both increases and decreases in the PAC from the *pre* to *post* condition, and

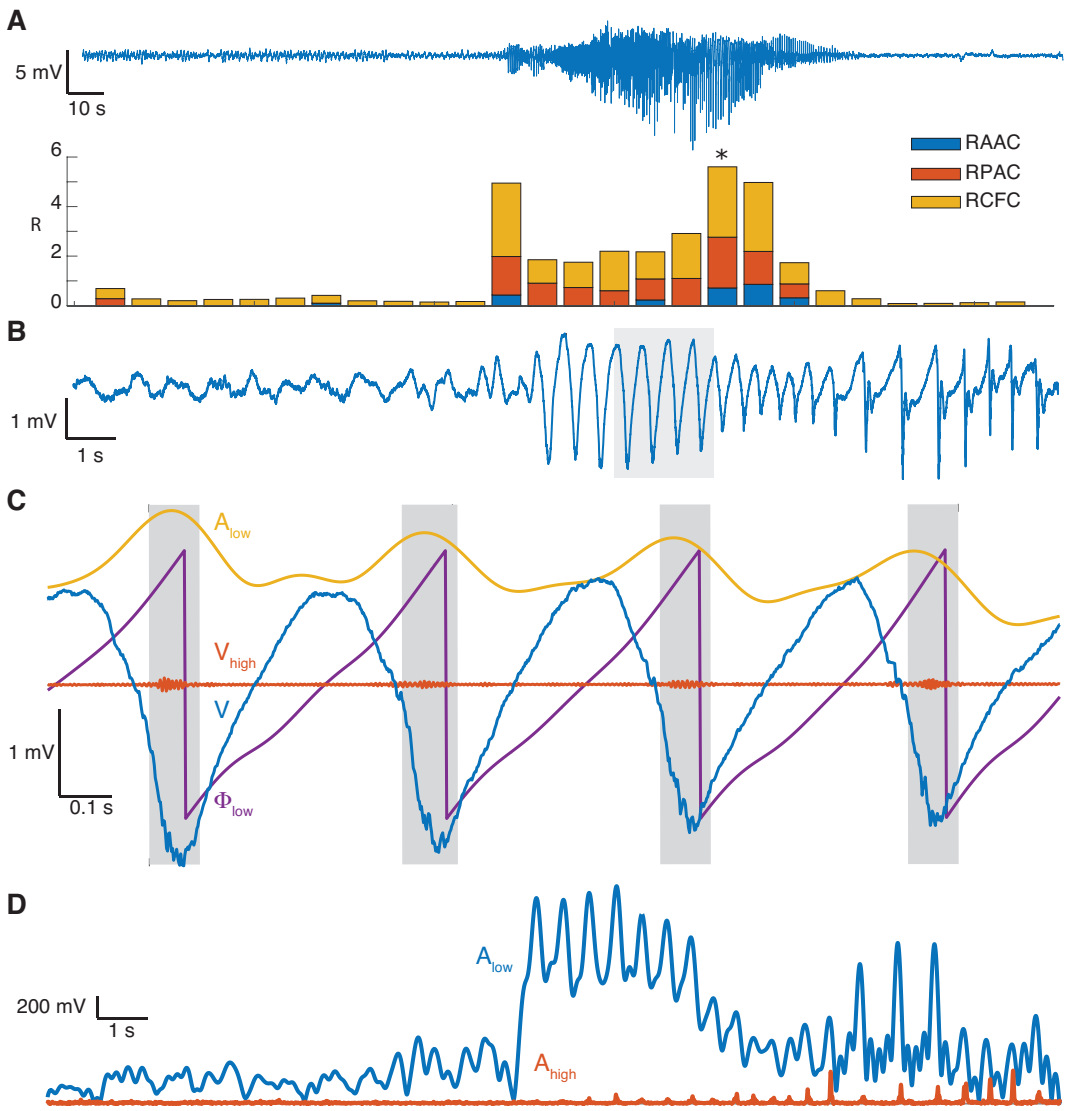

Figure 9. The CFC model detects cross-frequency coupling in an *in vivo* human recording. **(A)** Voltage recording from one MEA electrode over the course of seizure, and $\mathbf{R}_{\mathrm{PAC}}$, $\mathbf{R}_{\mathrm{AAC}}$, and $\mathbf{R}_{\mathrm{CFC}}$ values for 20 s segments of the trace. **(B)** Voltage trace corresponding to time segment (*) from (A). The gray-shaded time interval is analyzed in (C). **(C)** A subinterval of the voltage data (blue), along with V_{high} (red), A_{low} (yellow), and ϕ_{low} (purple). Grey shaded areas indicate increases in V_{high} when $\phi_{\mathrm{low}} = 0$. **(D)** A_{low} (blue) and A_{high} (red) for the 20 s segment in (B). A_{high} increases with A_{low} over time.

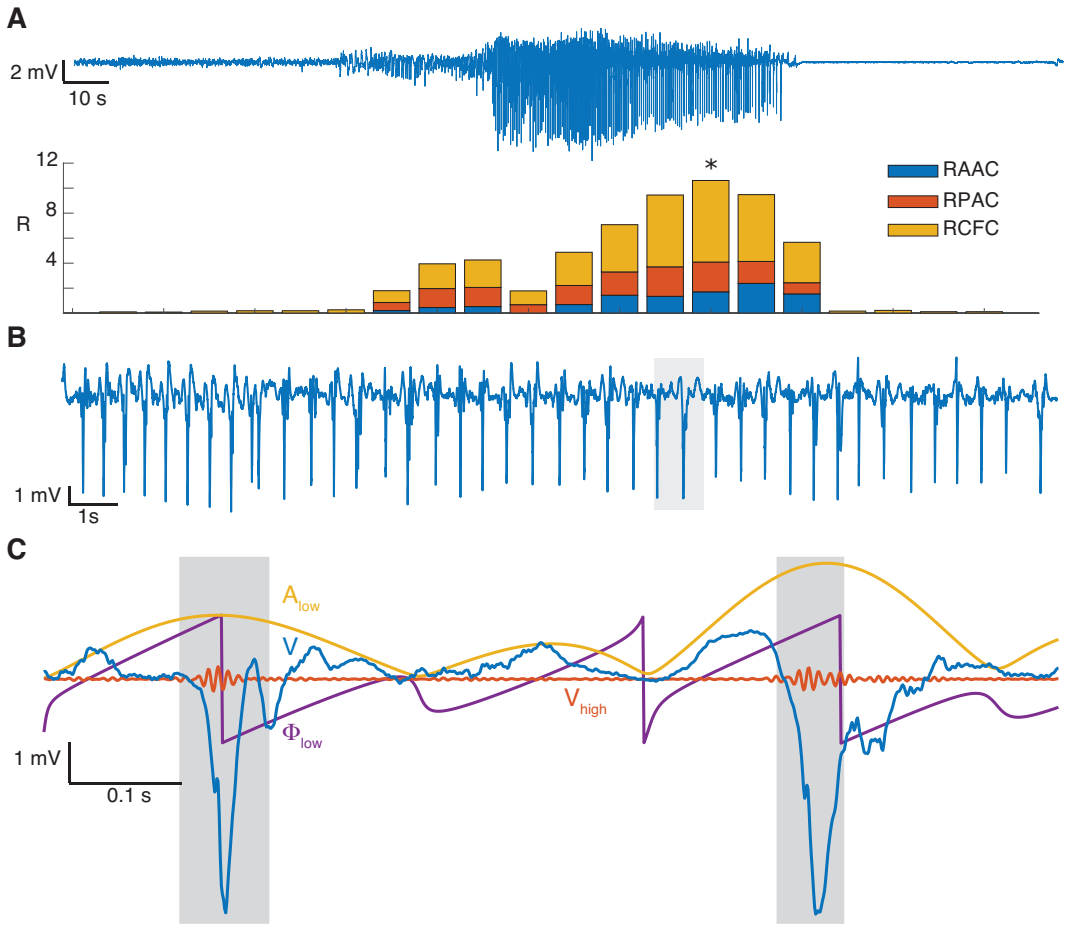

Figure 10. The CFC model detects cross-frequency coupling in a second *in vivo* human recordings. **(A)** Voltage recording from one MEA electrode over the course of seizure, and $\mathbf{R}_{\mathrm{PAC}}$, $\mathbf{R}_{\mathrm{AAC}}$, and $\mathbf{R}_{\mathrm{CFC}}$ values for 20 s segments of the trace. **(B)** Voltage trace corresponding to time segment (*) from (A). The gray-shaded time interval is analyzed in (C). **(C)** A subinterval of the voltage data (blue), along with V_{high} (red), A_{low} (yellow), and ϕ_{low} (purple). Grey shaded areas indicate increases in V_{high} when $\phi_{\mathrm{low}} = 0$ and A_{low} is large.

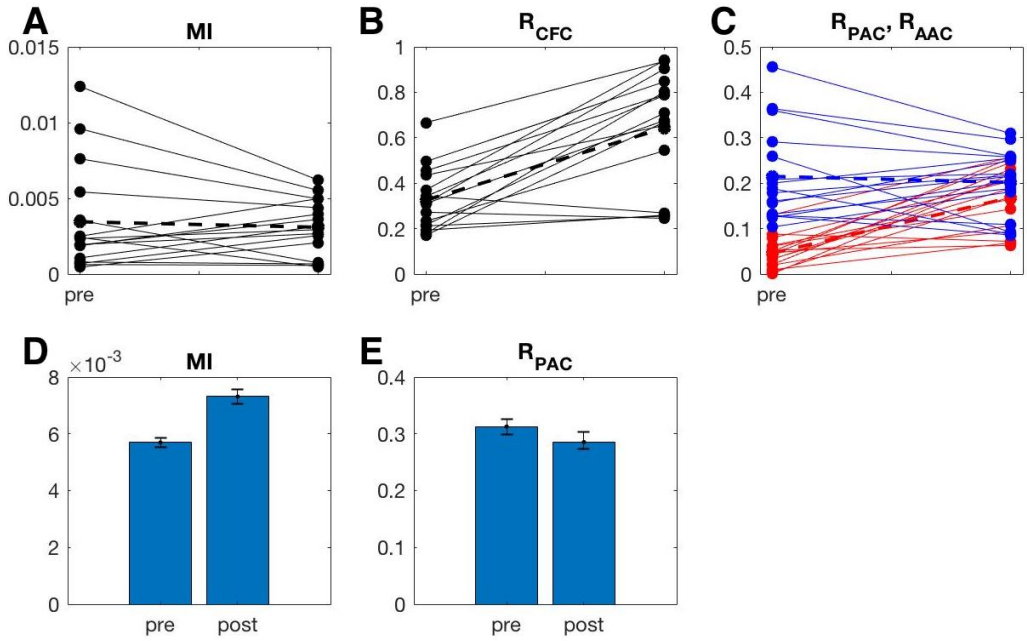

Figure 11. Measures of cross-frequency coupling across *pre* and *post* conditions **(A-C)** between IL and BLA regions, using modulation index, $\mathbf{R}_{\text{CFC}}$, and $\mathbf{R}_{\text{PAC}}$ and $\mathbf{R}_{\text{AAC}}$, and **(D-E)** for a single electrode using $\mathbf{R}_{\text{PAC}}$ and modulation index.

that the average change in **MI** across all 16 pairs is negligible ($p = 0.72$) (Figure 11A). However, using $\mathbf{R}_{\text{CFC}}$, we detect a notable increase in CFC from *pre* to *post* ($p < 0.001$) (Figure 11B). To determine which aspects of coupling impact the CFC, we examine $\mathbf{R}_{\text{PAC}}$ and $\mathbf{R}_{\text{AAC}}$ (Figure 11C). We find that the average $\mathbf{R}_{\text{PAC}}$ remains nearly constant across the *pre* and *post* conditions, similar to the **MI** $p = 0.68$. However, the average $\mathbf{R}_{\text{AAC}}$ increases significantly $(p < 0.001)$. Hence, we conclude that the increase in $\mathbf{R}_{\text{CFC}}$ from the *pre* to *post* condition results specifically from an increase in AAC.

We next consider an example of intra-electrode coupling, i.e. for a single electrode we measure the coupling between its low frequency (5-8 Hz) and high frequency (70-110 Hz) component. As both $\mathbf{R}_{\text{PAC}}$ and **MI** measure phase-amplitude coupling, we expect a similar change in both measures from the *pre* to *post* condition. However, while $\mathbf{R}_{\text{PAC}}$ decreases, **MI** increases (Figure 11D-E).

While a difference in $\mathbf{R}_{\text{PAC}}$ exists, the magnitude of this difference is small (Figure 11E). To test whether $\mathbf{R}_{\text{PAC}}$ changes across conditions, we implement a natural extension of the proposed framework. To do so we first concatenate the recordings for a given electrode from the *pre* condition V_{pre} and *post* condition V_{post} to create a new signal V^*:

$$V^* = [V_{\text{pre}}, V_{\text{post}}]. \tag{10}$$

From V^*, we obtain the corresponding high frequency signal V^*_{high} and low frequency signal V^*_{low}, and subsequently the high frequency amplitude A^*_{high}, low frequency phase ϕ^*_{low}, and low frequency amplitude A^*_{low}. We then use these data to generate a new model:

$$\begin{aligned} &A^*_{\text{high}} | \phi^*_{\text{low}}, A^*_{\text{low}}, P \sim \text{Gamma}[\mu, \nu], \\ &\log \mu = \sum_{k=1}^{n} \beta_k f_k(\phi^*_{\text{low}}) + \beta_{n+1} A^*_{\text{low}} + \beta_{n+2} A^*_{\text{low}} \sin(\phi^*_{\text{low}}) + \beta_{n+3} A^*_{\text{low}} \cos(\phi^*_{\text{low}}) + \sum_{j=1}^{n} P_j \beta_j f_j(\phi^*_{\text{low}}), \end{aligned} \tag{11}$$

where P is an indicator vector that signifies whether the signal is in the *post* condition ($P_j = 1$) or the *pre* condition ($P_j = 0$). The final term $\sum_{j=1}^{n} P_j \beta_j f_j(\phi^*_{\text{low}})$ models the effect of the *post* condition

on PAC: if each $\beta_j = 0$, then there is no effect; if $\beta_j > 0$ then the impact of phase $f_j(\phi^*_{\text{low}})$ on A_{high} increases in the *post* condition; if $\beta_j < 0$ then the impact of phase $f_j(\phi^*_{\text{low}})$ on A_{high} decreases in the *post* condition.

Fitting this new model to the rodent *in vivo* data, we then perform a χ^2 test to compare Model 2 and Model 11 with 10 degrees of freedom, corresponding to new indicator terms. We obtain $p \approx 0$, and therefore reject the null hypothesis that $\beta_j = 0$ for all j; we conclude that the condition - *pre* or *post* - impacts the PAC. Investigating each value in the indicator vector, we find $\beta_j < 0$ for all j ($p < 0.001$). We therefore conclude that, when in the *post* condition, there is a decrease in PAC. This analysis supports our initial conclusion based on visual inspection of $\mathbf{R}_{\text{PAC}}$ (Figure 11E). We note that this change is not consistent with the **MI** result (Figure 11D). While the true change in $\mathbf{R}_{\text{PAC}}$ remains unknown in these *in vivo* data, this example illustrates an advantage of the proposed framework: the generalized linear model is easily extended to test the significance of additional covariates motivated by the experiment. While here we applied an indicator function for condition on PAC, many other covariates exist (e.g., sex, stimulus parameters) whose effect on PAC, AAC, or both can be explored in this principled statistical framework.

Discussion

In this paper, we proposed a new method for measuring cross-frequency coupling that accounts for both phase-amplitude coupling and amplitude-amplitude coupling, along with a principled statistical modeling framework to assess the significance of this coupling. We have shown that this method effectively detects CFC, both as PAC and AAC, and is more sensitive to weak PAC obscured by or coupled to low-frequency amplitude fluctuations. Compared to an existing method, the modulation index [57], the newly proposed method more accurately detects scenarios in which PAC is coupled to the low-frequency amplitude. Finally, we applied this method to *in vivo* data to illustrate examples of PAC and AAC in real systems, and show how to extend the modeling framework to include a new covariate.

One of the most important features of the new method is an increased ability to detect weak PAC coupled to AAC. For example, when sparse PAC events occur only when the low frequency amplitude (A_{low}) is large, the proposed method detects this coupling while other methods not accounting for A_{low} miss it. While PAC often occurs in neural data, and has been associated with numerous neurological functions [10, 26], the simultaneous occurrence of PAC and AAC is less well studied [44]. Here, we showed examples of simultaneous PAC and AAC recorded from human cortex during seizure, and we note that this phenomena has been simulated in other works [41].

While the exact mechanisms that support CFC are not well understood [26], the general mechanisms of low and high frequency rhythms have been proposed. Low frequency rhythms are associated with the aggregate activity of large neural populations and modulations of neuronal excitability [20, 62, 8], while high frequency rhythms provided a surrogate measure of neuronal spiking [48, 42, 23, 47, 69, 50, 49]. These two observations provide a physical interpretation for PAC: when a low frequency rhythm modulates the excitability of a neural population, we expect spiking to occur (i.e., an increase in A_{high}) at a particular phase of the low frequency rhythm (ϕ_{low}) when excitation is maximal. These notions also provide a physical interpretation for AAC: increases in A_{low} produce larger modulations in neural excitability, and therefore increased intervals of neuronal spiking (i.e., increases in A_{high}). Alternatively, decreases in A_{low} reduce excitability and neuronal spiking (i.e., decreases in A_{high}).

The function of concurrent PAC and AAC, both for healthy brain function and over the course of seizure as illustrated here, is not well understood. However, we note that over the course of seizure, particularly at termination, PAC and AAC are both present. As PAC occurs normally in healthy brain signals, for example during working memory, neuronal computation, communication, learning and emotion [58, 30, 10, 18, 33, 39, 32, 31, 54], these preliminary results may suggest a pathological aspect of strong AAC occurring concurrently with PAC.

Proposed functions of PAC include multi-item encoding, long-distance communication, and

sensory parsing [26]. Each of these functions takes advantage of the low frequency phase, encoding different objects or pieces of information in distinct phase intervals of ϕ_{low}. PAC can be interpreted as a type of focused attention; A_{high} modulation occurring only in a particular interval of ϕ_{low} organizes neural activity - and presumably information - into discrete packets of time. Similarly, a proposed function of AAC is to encode the number of represented items, or the amount of information encoded in the modulated signal [26]. A pathological increase in AAC may support the transmission of more information than is needed, overloading the communication of relevant information with irrelevant noise. The attention-based function of PAC, i.e. having reduced high frequency amplitude at phases not containing the targeted information, may be lost if the amplitude of the high frequency oscillation is increased across wide intervals of low frequency phase.

Like all measures of CFC, the proposed method possesses specific limitations. We discuss three limitations here. First, the choice of spline basis to represent the low frequency phase may be inaccurate, for example if the PAC changes rapidly with ϕ_{low}. Second, the value of $\mathbf{R}_{\text{AAC}}$ depends on the range of A_{low} observed. This is due to the linear relationship between A_{low} and A_{high} in the AAC model, which causes the maximum distance between the surfaces S_{AAC} and S_{CFC} to occur at the largest or smallest value of A_{low}. To mitigate the impact of extreme A_{low} values on $\mathbf{R}_{\text{AAC}}$, we evaluate the surfaces S_{AAC} and S_{CFC} over the 5th to 95th quantiles of A_{low}. We note that an alternative metric of AAC could instead evaluate the slope of the S_{AAC} surface; to maintain consistency of the PAC and AAC measures, we chose not to implement this alternative measure here. Third, the frequency bands for V_{high} and V_{low} must be established before **R** values are calculated. Hence, if the wrong frequency bands are chosen, coupling may be missed. It is possible, though computationally expensive, to scan over all reasonable frequency bands for both V_{high} and V_{low}, calculating **R** values for each frequency band pair.

The proposed method can easily be extended by inclusion of additional predictors in the GLM. Polynomial A_{low} predictors, rather than the current linear A_{low} predictors, may better capture the relationship between A_{low} and A_{high}. One could also include different types of covariates, for example classes of drugs administered to a patient, or time since an administered stimulus during an experiment. The code developed to implement the method is flexible and modular, which facilitates the addition and removal of predictors, while utilizing the same statistical modeling framework to assess the significance of each predictor. This modular code, available at https://github.com/Eden-Kramer-Lab/GLM-CFC, also allows the user to change latent assumptions, such as choice of frequency bands and filtering method. The code is freely available for reuse and further development.

Rhythms, and particularly the interactions of different frequency rhythms, are an important component for a complete understanding of neural activity. While the mechanisms and functions of some rhythms are well understood, how and why rhythms interact remains uncertain. A first step in addressing these uncertainties is the application of appropriate data analysis tools. Here we provide a new tool to measure coupling between different brain rhythms: the method utilizes a statistical modeling framework that is flexible and captures subtle differences in cross-frequency coupling. We hope that this method will better enable practicing neuroscientists to measure and relate brain rhythms, and ultimately better understand brain function and interactions.

Acknowledgements

This work was supported in part by the National Science Foundation Award #1451384.

References

[1] Agarwal, G., Stevenson, I. H., Berényi, A., Mizuseki, K., Buzsáki, G., and Sommer, F. T. (2014). Spatially distributed local fields in the hippocampus encode rat position. *Science*, 344(6184):626.

[2] Aru, J., Aru, J., Priesemann, V., Wibral, M., Lana, L., Pipa, G., Singer, W., and Vicente, R. (2015). Untangling cross-frequency coupling in neuroscience. *Current Opinion in Neurobiology*, 31:51–61.

[3] Başar, E., Schmiedt-Fehr, C., Mathes, B., Femir, B., Emek-Savaş, D. D., Tülay, E., Tan, D., Düzgün, A., Güntekin, B., Özerdem, A., Yener, G., and Başar-Eroğlu, C. (2016). What does the broken brain say to the neuroscientist? oscillations and connectivity in schizophrenia, alzheimer's disease, and bipolar disorder. *International Journal of Psychophysiology*, 103:135–148.

[4] Blackwood, E., Lo, M., and Widge, S. A. (2018). Continuous phase estimation for phase-locked neural stimulation using an autoregressive model for signal prediction*. In *2018 40th Annual International Conference of the IEEE Engineering in Medicine and Biology Society (EMBC)*, pages 4736–4739.

[5] Börgers, C., Epstein, S., and Kopell, N. J. (2008). Gamma oscillations mediate stimulus competition and attentional selection in a cortical network model. *Proceedings of the National Academy of Sciences of the United States of America*, 105(46):18023–18028.

[6] Bragin, A., Jando, G., Nadasdy, Z., Hetke, J., Wise, K., and Buzsaki, G. (1995). Gamma (40-100 hz) oscillation in the hippocampus of the behaving rat. *The Journal of Neuroscience*, 15(1):47.

[7] Bruns, A. and Eckhorn, R. (2004). Task-related coupling from high- to low-frequency signals among visual cortical areas in human subdural recordings. *International Journal of Psychophysiology*, 51(2):97–116.

[8] Buzsáki, G. and Draguhn, A. (2004). Neuronal oscillations in cortical networks. *Science*, 304(5679):1926.

[9] Canolty, R. T., Edwards, E., Dalal, S. S., Soltani, M., Nagarajan, S. S., Kirsch, H. E., Berger, M. S., Barbaro, N. M., and Knight, R. T. (2006). High gamma power is phase-locked to theta oscillations in human neocortex. *Science*, 313(5793):1626.

[10] Canolty, R. T. and Knight, R. T. (2010). The functional role of cross-frequency coupling. *Trends in Cognitive Sciences*, 14(11):506–515.

[11] Chrobak, J. J. and Buzsáki, G. (1998). Gamma oscillations in the entorhinal cortex of the freely behaving rat. *The Journal of Neuroscience*, 18(1):388.

[12] Cohen, M. X. (2008). Assessing transient cross-frequency coupling in eeg data. *Journal of Neuroscience Methods*, 168(2):494–499.

[13] Cohen, M. X. and Davachi, L. (2017). Multivariate cross-frequency coupling via generalized eigendecomposition. *eLife*, 6:e21792.

[14] Cole, S. R. and Voytek, B. (2017). Brain oscillations and the importance of waveform shape. *Trends in Cognitive Sciences*, 21(2):137–149.

[15] Colgin, L. L., Denninger, T., Fyhn, M., Hafting, T., Bonnevie, T., Jensen, O., Moser, M.-B., and Moser, E. I. (2009). Frequency of gamma oscillations routes flow of information in the hippocampus. *Nature*, 462:353.

[16] Csicsvari, J., Jamieson, B., Wise, K. D., and Buzsáki, G. (2003). Mechanisms of gamma oscillations in the hippocampus of the behaving rat. *Neuron*, 37(2):311–322.

[17] Dean, H. L., Hagan, M. A., and Pesaran, B. (2012). Only coherent spiking in posterior parietal cortex coordinates looking and reaching. *Neuron*, 73(4):829–841.

[18] Dejean, C., Courtin, J., Karalis, N., Chaudun, F., Wurtz, H., Bienvenu, T. C. M., and Herry, C. (2016). Prefrontal neuronal assemblies temporally control fear behaviour. *Nature*, 535:420 EP –.

[19] DH, M. and VS, S. (2015). Neural oscillations and synchrony in brain dysfunction and neuropsychiatric disorders: It's about time. *JAMA Psychiatry*, 72(8):840–844.

[20] Engel, A. K., Fries, P., and Singer, W. (2001). Dynamic predictions: Oscillations and synchrony in top–down processing. *Nature Reviews Neuroscience*, 2:704 EP –.

[21] Florian, M., Juergen, F., Nikolai, A., Bernd, W., Klaus, L., E., E. C., and Guillén, F. (2005). Phase/amplitude reset and theta–gamma interaction in the human medial temporal lobe during a continuous word recognition memory task. *Hippocampus*, 15(7):890–900.

[22] Fries, P., Nikolić, D., and Singer, W. (2007). The gamma cycle. *Trends in Neurosciences*, 30(7):309–316.

[23] Fries, P., Reynolds, J. H., Rorie, A. E., and Desimone, R. (2001). Modulation of oscillatory neuronal synchronization by selective visual attention. *Science*, 291(5508):1560.

[24] Gordon, J. A. (2016). On being a circuit psychiatrist. *Nature Neuroscience*, 19:1385 EP –.

[25] Hawellek, D. J., Wong, Y. T., and Pesaran, B. (2016). Temporal coding of reward-guided choice in the posterior parietal cortex. *Proceedings of the National Academy of Sciences*, 113(47):13492.

[26] Hyafil, A., Giraud, A.-L., Fontolan, L., and Gutkin, B. (2015). Neural cross-frequency coupling: Connecting architectures, mechanisms, and functions. *Trends in Neurosciences*, 38(11):725–740.

[27] Jensen, O., Gips, B., Bergmann, T. O., and Bonnefond, M. (2014). Temporal coding organized by coupled alpha and gamma oscillations prioritize visual processing. *Trends in Neurosciences*, 37(7):357–369.

[28] Jensen, O. and Lisman, J. E. (2000). Position reconstruction from an ensemble of hippocampal place cells: Contribution of theta phase coding. *Journal of Neurophysiology*, 83(5):2602–2609.

[29] Jensen, O. and Mazaheri, A. (2010). Shaping functional architecture by oscillatory alpha activity: Gating by inhibition. *Frontiers in Human Neuroscience*, 4:186.

[30] Jensen, O., Spaak, E., and Park, H. (2016). Discriminating valid from spurious indices of phase-amplitude coupling. *eNeuro*, 3(6):ENEURO.0334–16.2016.

[31] John, L. (2005). The theta/gamma discrete phase code occuring during the hippocampal phase precession may be a more general brain coding scheme. *Hippocampus*, 15(7):913–922.

[32] Jones, M. W. and Wilson, M. A. (2005). Theta rhythms coordinate hippocampal–prefrontal interactions in a spatial memory task. *PLOS Biology*, 3(12):e402–.

[33] Karalis, N., Dejean, C., Chaudun, F., Khoder, S., Rozeske, R. R., Wurtz, H., Bagur, S., Benchenane, K., Sirota, A., Courtin, J., and Herry, C. (2016). 4-hz oscillations synchronize prefrontal–amygdala circuits during fear behavior. *Nature Neuroscience*, 19:605 EP –.

[34] Kopell, N., Ermentrout, G. B., Whittington, M. A., and Traub, R. D. (2000). Gamma rhythms and beta rhythms have different synchronization properties. *Proceedings of the National Academy of Sciences of the United States of America*, 97(4):1867–1872.

[35] Kramer, M. A. and Eden, U. T. (2013). Assessment of cross-frequency coupling with confidence using generalized linear models. *Journal of Neuroscience Methods*, 220(1):64–74.

[36] Lachaux, J. P., Rodriguez, E., Martinerie, J., and Varela, F. J. J. (1999). *Measuring Phase Synchrony in Brain Signals*, volume 8.

[37] Lakatos, P., Karmos, G., Mehta, A. D., Ulbert, I., and Schroeder, C. E. (2008). Entrainment of neuronal oscillations as a mechanism of attentional selection. *Science*, 320(5872):110.

[38] Lakatos, P., Shah, A. S., Knuth, K. H., Ulbert, I., Karmos, G., and Schroeder, C. E. (2005). An oscillatory hierarchy controlling neuronal excitability and stimulus processing in the auditory cortex. *Journal of Neurophysiology*, 94(3):1904–1911.

[39] Likhtik, E., Stujenske, J. M., A Topiwala, M., Harris, A. Z., and Gordon, J. A. (2013). Prefrontal entrainment of amygdala activity signals safety in learned fear and innate anxiety. *Nature Neuroscience*, 17:106 EP –.

[40] Mann, E. O. and Mody, I. (2009). Control of hippocampal gamma oscillation frequency by tonic inhibition and excitation of interneurons. *Nature Neuroscience*, 13:205 EP –.

[41] Mazzoni, A., Whittingstall, K., Brunel, N., Logothetis, N. K., and Panzeri, S. (2010). Understanding the relationships between spike rate and delta/gamma frequency bands of lfps and eegs using a local cortical network model. *NeuroImage*, 52(3):956–972.

[42] Mukamel, R., Gelbard, H., Arieli, A., Hasson, U., Fried, I., and Malach, R. (2005). Coupling between neuronal firing, field potentials, and fmri in human auditory cortex. *Science*, 309(5736):951.

[43] Onslow, A. C. E., Bogacz, R., and Jones, M. W. (2011). Quantifying phase–amplitude coupling in neuronal network oscillations. *Progress in Biophysics and Molecular Biology*, 105(1):49–57.

[44] Osipova, D., Hermes, D., and Jensen, O. (2008). Gamma power is phase-locked to posterior alpha activity. *PLOS ONE*, 3(12):e3990–.

[45] Penny, W. D., Duzel, E., Miller, K. J., and Ojemann, J. G. (2008). Testing for nested oscillation. *Journal of Neuroscience Methods*, 174(1):50–61.

[46] Pesaran, B., Nelson, M. J., and Andersen, R. A. (2008). Free choice activates a decision circuit between frontal and parietal cortex. *Nature*, 453:406 EP –.

[47] Pesaran, B., Pezaris, J. S., Sahani, M., Mitra, P. P., and Andersen, R. A. (2002). Temporal structure in neuronal activity during working memory in macaque parietal cortex. *Nature Neuroscience*, 5:805 EP –.

[48] Rasch, M. J., Gretton, A., Murayama, Y., Maass, W., and Logothetis, N. K. (2008). Inferring spike trains from local field potentials. *Journal of Neurophysiology*, 99(3):1461–1476.

[49] Ray, S., Hsiao, S. S., Crone, N. E., Franaszczuk, P. J., and Niebur, E. (2008). Effect of stimulus intensity on the spike–local field potential relationship in the secondary somatosensory cortex. *The Journal of Neuroscience*, 28(29):7334.

[50] Ray, S. and Maunsell, J. H. R. (2011). Different origins of gamma rhythm and high-gamma activity in macaque visual cortex. *PLOS Biology*, 9(4):e1000610–.

[51] Scheffer-Teixeira, R., Belchior, H., Leão, R. N., Ribeiro, S., and Tort, A. B. L. (2013). On high-frequency field oscillations (>100 hz) and the spectral leakage of spiking activity. *The Journal of Neuroscience*, 33(4):1535.

[52] Shirvalkar, P. R., Rapp, P. R., and Shapiro, M. L. (2010). Bidirectional changes to hippocampal theta–gamma comodulation predict memory for recent spatial episodes. *Proceedings of the National Academy of Sciences*, 107(15):7054.

[53] Siegel, M., Warden, M. R., and Miller, E. K. (2009). Phase-dependent neuronal coding of objects in short-term memory. *Proceedings of the National Academy of Sciences*, 106(50):21341.

[54] Sirota, A., Montgomery, S., Fujisawa, S., Isomura, Y., Zugaro, M., and Buzsáki, G. (2008). Entrainment of neocortical neurons and gamma oscillations by the hippocampal theta rhythm. *Neuron*, 60(4):683–697.

[55] Spaak, E., Bonnefond, M., Maier, A., Leopold, D. A., and Jensen, O. (2012). Layer-specific entrainment of gamma-band neural activity by the alpha rhythm in monkey visual cortex. *Current Biology*, 22(24):2313–2318.

[56] Theiler, J., Eubank, S., Longtin, A., Galdrikian, B., and Doyne Farmer, J. (1992). Testing for nonlinearity in time series: the method of surrogate data. *Physica D: Nonlinear Phenomena*, 58(1):77–94.

[57] Tort, A. B. L., Komorowski, R., Eichenbaum, H., and Kopell, N. (2010). Measuring phase-amplitude coupling between neuronal oscillations of different frequencies. *Journal of Neurophysiology*, 104(2):1195–1210.

[58] Tort, A. B. L., Komorowski, R. W., Manns, J. R., Kopell, N. J., and Eichenbaum, H. (2009). Theta–gamma coupling increases during the learning of item–context associations. *Proceedings of the National Academy of Sciences*, 106(49):20942.

[59] Tort, A. B. L., Kramer, M. A., Thorn, C., Gibson, D. J., Kubota, Y., Graybiel, A. M., and Kopell, N. J. (2008). Dynamic cross-frequency couplings of local field potential oscillations in rat striatum and hippocampus during performance of a t-maze task. *Proceedings of the National Academy of Sciences*, 105(51):20517.

[60] van Wijk, B., Jha, A., Penny, W., and Litvak, V. (2015). Parametric estimation of cross-frequency coupling. *Journal of Neuroscience Methods*, 243:94–102.

[61] Vanhatalo, S., Palva, J. M., Holmes, M. D., Miller, J. W., Voipio, J., and Kaila, K. (2004). Infraslow oscillations modulate excitability and interictal epileptic activity in the human cortex during sleep. *Proceedings of the National Academy of Sciences of the United States of America*, 101(14):5053.

[62] Varela, F., Lachaux, J.-P., Rodriguez, E., and Martinerie, J. (2001). The brainweb: Phase synchronization and large-scale integration. *Nature Reviews Neuroscience*, 2:229 EP –.

[63] Vinck, M., Lima, B., Womelsdorf, T., Oostenveld, R., Singer, W., Neuenschwander, S., and Fries, P. (2010). Gamma-phase shifting in awake monkey visual cortex. *The Journal of Neuroscience*, 30(4):1250.

[64] von Stein, A. and Sarnthein, J. (2000). Different frequencies for different scales of cortical integration: from local gamma to long range alpha/theta synchronization. *International Journal of Psychophysiology*, 38(3):301–313.

[65] Voytek, B., D'Esposito, M., Crone, N., and Knight, R. T. (2013). A method for event-related phase/amplitude coupling. *NeuroImage*, 64:416–424.

[66] Voytek, B. and Knight, R. T. (2015). Dynamic network communication as a unifying neural basis for cognition, development, aging, and disease. *Biological Psychiatry*, 77(12):1089–1097.

[67] Wagner, F. B., Eskandar, E. N., Cosgrove, G. R., Madsen, J. R., Blum, A. S., Potter, N. S., Hochberg, L. R., Cash, S. S., and Truccolo, W. (2015). Microscale spatiotemporal dynamics during neocortical propagation of human focal seizures. *NeuroImage*, 122:114–130.

[68] Weiss, S. A., Lemesiou, A., Connors, R., Banks, G. P., McKhann, G. M., Goodman, R. R., Zhao, B., Filippi, C. G., Nowell, M., Rodionov, R., Diehl, B., McEvoy, A. W., Walker, M. C., Trevelyan, A. J., Bateman, L. M., Emerson, R. G., and Schevon, C. A. (2015). Seizure localization using ictal phase-locked high gamma. *Neurology*, 84(23):2320–2328.

[69] Whittingstall, K. and Logothetis, N. K. (2009). Frequency-band coupling in surface eeg reflects spiking activity in monkey visual cortex. *Neuron*, 64(2):281–289.

[70] Whittington, M. A., Cunningham, M. O., LeBeau, F. E. N., Racca, C., and Traub, R. D. (2010). Multiple origins of the cortical gamma rhythm. *Developmental Neurobiology*, 71(1):92–106.

[71] Whittington, M. A., Traub, R. D., Kopell, N., Ermentrout, B., and Buhl, E. H. (2000). Inhibition-based rhythms: experimental and mathematical observations on network dynamics. *International Journal of Psychophysiology*, 38(3):315–336.

[72] Widge, A. S., Ellard, K. K., Paulk, A. C., Basu, I., Yousefi, A., Zorowitz, S., Gilmour, A., Afzal, A., Deckersbach, T., Cash, S. S., Kramer, M. A., Eden, U. T., Dougherty, D. D., and Eskandar, E. N. (2017). Treating refractory mental illness with closed-loop brain stimulation: Progress towards a patient-specific transdiagnostic approach. *Experimental Neurology*, 287:461–472.

[73] Wong, Y. T., Fabiszak, M. M., Novikov, Y., Daw, N. D., and Pesaran, B. (2016). Coherent neuronal ensembles are rapidly recruited when making a look-reach decision. *Nature neuroscience*, 19(2):327–334.